Structural and optical properties of bismuth vanadate

A

Dissertation

Submitted for partial fulfillment of the requirement for the award of the degree of

Master of Science

In

Physics

Under the supervision of

Dr. Kulvir Singh

(Associate Professor & Head)

Submitted by

Malti Devi

Roll No.-**301004005**

School of Physics and Materials Science

Thapar University

Patiala (Punjab) - 147004

July, 2012

CERTIFICATE

This is to certify that this thesis entitled **"Study of structural and optical properties of bismuth vanadate"** which is being submitted by Malti Devi in fulfillment of the requirement for the award of the degree of master of science in School of Physics and Materials Science, Thapar University, Patiala (Punjab), is record of candidate's own work carried out by her under my supervision and guidance. The matter embodied in this dissertation has not been submitted in part or full to any other university or institute for the award of any degree.

Dr. Kulvir Singh

(Associate professor and Head)

SPMS, Thapar University

Patiala

Countersigned By:

Dr. Kulvir Singh

(Associate professor and Head)
SPMS, Thapar University,
Patiala.

Dr. S.K. Mohapatra

Dean, Academic Affairs
Thapar University,
Patiala.

ACKNOWLEDGEMENT

I express my deep gratitude and respects to my guide **Dr. Kulvir Singh**, **Associate Professor and Head, School of Physics and Materials Science at THAPAR UNIVERSITY, PATIALA.** I got the valuable guidance, strong motivation and constant encouragement during thesis work. The work presented here could not have been accomplished without his motivating supervision and practical admiration during my thesis work.

I am incredibly grateful to **Dr. K. K. Raina, Deputy Director and Distinguished Professor,** for their kind support. I express my sincere thanks to **Dr. B. Chudasama**, who provides the experimental facility as well as guide me during my work. My sincere thank to **Dr. O.P. Pandey**, and **Ms. Loveleen Kaur Brar** for their valuable suggestions and motivation during my thesis work.

It gives me immense pleasure to express my special thanks to **Ms. Samita Thakur** who always took keen interest in my work and also because of her I am able to complete my work successfully.

I am grateful to **Ms. Deepti, Mr. Gourav, Mr. Param, Mr. Kapil,** and all research scholars of the School of Physics and Materials Science department who help me directly or indirectly during the project work. I owe my sincere thanks to all the staff members of **School of Physics and Materials Science** for their support and encouragement.

I would also like to thank my friends Ms. Anmol Preet Kaur, Ms. Shivani Sharma, Ms. Lavlesh Kumari, Ms. Navjot Kaur Virk, Ms. Yoshita Ahuja for extending their whole hearted support.

Last but not the least; I would like to thank my parents, my brother for their moral support that kept my spirit up during the endeavor.

Malti Devi

Ms. Malti Devi

List of content

Page No.

Chapter -1 **1.**

1.1. Inroduction 1.

1.2. $Bi_2O_3 – V_2O_5$ system 1.

1.2.1. Properties of Bi_2O_3 system

1.2.1.1. Ferroelectric and ferroelastic properties 2.

1.2.1.2. Conductivity 4.

1.2.1.3. Optical properties 5.

1.3. Bismuth vanadate 5.

1.3.1. Structural aspects 6.

1.3.1.1. Fluorite structure 6.

1.3.1.2. Aurivillius structure 8.

1.3.2. Phase classification 9.

Chapter-2 **11.**

Literature review

Chapter-3 **18.**

Experimental techniques and measurements

3.1. Sample preparation 18.

3.2. Characterization 19.

3.2.1. X- rays diffraction 19.

3.2.2. Fourier transform infrared spectroscopy 20.

3.2.3. Scanning electron microscope 21.

3.2.4. Ultraviolet–visible spectroscopy 22.

Chapter-4 **24.**

Result and discussion 24.

Conclusion and future scope 38.

References 39.

PREFACE

The Bismuth vanadate ($Bi_{4-x}M_xV_2O_{11}$, M= Gd, La, $0 \leq x \geq 0.4$) powders were synthesized by solid state reaction method with dopants Gd^{3+} and La^{3+} on the bismuth site. To confirm the phases, the samples were investigated by X-ray diffraction. The morphology of $Bi_{4-x}M_xV_2O_{11}$ samples were studied by scanning electron microscope (SEM). The average grain size of the samples vary in the range of 3 to 7 μm. The elemental composition of $Bi_{4-x}M_xV_2O_{11}$ was measured by energy dispersive X- ray spectroscopy (EDS). The specimens were also studied by Fourier transform infrared spectroscopy (FTIR) and UV-Visible spectroscopy to identifying types of chemical bonds, unknown materials and measuring the response of a sample to ultraviolet and visible range of electromagnetic radiations. The estimated band gap of La-doped and Gd- doped samples are lies in the range of 1.86 to 3.11eV, and 2.18 to 1.87 eV respectively.

LIST OF FIGURE

Figure 1.1: Distorted monocapped Trigonal Prism Coordination for Bismuth.

Figure 1.2: $(BiO_2)^-$ Chain Configuration for Bismuth.

Figure 1.3: $(Bi_2O_2)^{2+}$ Chain Configuration for Bismuth.

Figure 1.4: Unit cell for the fluorite (AO_2) structure.

Figure 1.5: Aurivillius structure of bismuth Vanadate.

Figure 1.6: Unusual Five Short and two long coordination for Bismuth.

Figure 3.1: Illustration of the Bragg's law.

Figure 3.2: Set up of FTIR.

Figure 3.3: Apparatus of scanning electron microscope.

Figure 3.4: Set up of UV-Vis spectroscopy.

Figure 4.1: X- ray spectra of $Bi_{4-x}Gd_xV_2O_{11}$ ($0\leq x\geq 0.4$); (✡) supperlattice reflection.

Figure 4.2: X- ray spectra of Bi4-xLaxV2O11 ($0\leq x\geq 0.4$) ;(✡) supperlattice reflection.

Figure 4.3: Variation of lattice parameters & volume with conc. of Gd, $Bi_{4-x}Gd_xV_2O_{11}$ ($0\leq x\geq 0.4$)

Figure 4.4: Variation of lattice parameters & volume with conc. of La, $Bi_{4-x}La_xV_2O_{11}$ ($0\leq x\geq 0.4$)

Figure 4.5: (a) & (b) SEM micrograph and (c) EDS, of $Bi_{3.9}Gd_{0.1}V_2O_{11.}$

Figure 4.6: (a) & (b) SEM micrograph and (c) EDS, of $Bi_{3.7}Gd_{0.3}V_2O_{11.}$

Figure 4.7: (a) & (b) SEM micrograph and (c) EDS of $Bi_{3.9}La_{0.1}V_2O_{11.}$

Figure 4.8: (a) and (b) SEM micrograph and (c) EDS, of $Bi_{3.7}La_{0.3}V_2O_{11.}$

Figure 4.9: FTIR spectra of $Bi_{4-x}Gd_xV_2O_{11}$ samples ($0\leq x\geq 0.4$).

Figure 4.10: FTIR spectra of $Bi_{4-x}La_xV_2O_{11}$ samples ($0\leq x\geq 0.4$).

Figure 4.11: UV- Vis spectra of $Bi_{4-x}Gd_xV_2O_{11}$ samples ($0\leq x\geq 0.4$).

Figure 4.12: UV- Vis spectra of $Bi_{4-x}La_xV_2O_{11}$ samples ($0\leq x\geq 0.4$).

LIST OF TABLES

Table 1: Lattice parameter of $Bi_{4-x}Gd_xV_2O_{11}$ and $Bi_{4-x}La_xV_2O_{11}$ ($0\leq x\geq 0.4$).

Table 2: The atomic percentage composition of $Bi_{4-x}Gd_xV_2O_{11}$(M=Gd, La at x=0.1,0.3).

Table 3: Infrared absorption bands and their assignments.

Table 4: Energy band gap of $Bi_{4-x}Gd_xV_2O_{11}$and $Bi_{4-x}La_xV_2O_{11}$ ($0\leq x\geq 0.4$).

CHAPTER-1

1.1. INTRODUCTION

Since long back, new materials have been synthesized for better scientific, engineering and technology properties. Bi_2O_3 is multifunctional materials which can be used in various properties. These properties can be enhanced by using various dopants and changing processing parameter. The most commonly used synthesis technique is solid states reaction method. New materials may require special synthesis techniques. Complex structures, both in three-dimensional framework and element composition need to be attempted. Many spectacular new materials are waiting to be uncovered and their properties will have a profound impact on science and technology. When new discoveries are made, they will be exploited to the fullest through systematic and applied studies. The goal is to make useful, inexpensive, nontoxic and easy to manufacture the new materials.

1.2. Bi_2O_3 based systems

Bi^{3+} has an electronic configuration of [Xe] $4f^{14}5d^{10}6s^2$. The $6s^2$ electrons are commonly referred to as the lone pair electrons. Hybridization of the 6s and 6p orbitals and the resulting lone electron pair yields some very interesting stereochemistry and steric related properties. Bismuth environments commonly have seven-fold coordination with some long and some short bonds due to the stereoactive lone pair of electrons.

These arrangements are found in solid-state materials and organometallics [1]. One common environment is the distorted monocapped trigonal prism or distorted monocapped octahedron as shown in **figure 1.1**. In this coordination strong bonds occur opposite to weak bonds and four intermediate bonds are found in the equatorial plane [2].

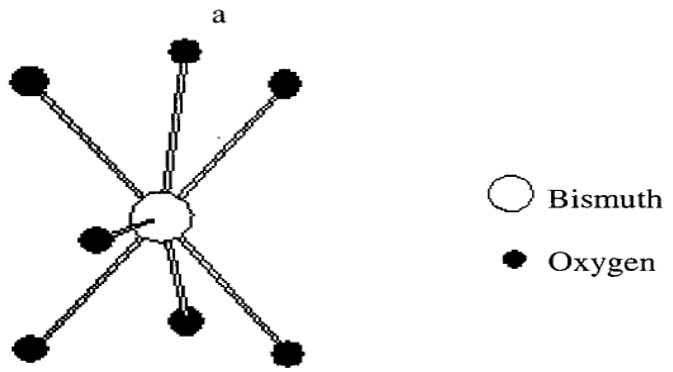

Figure 1.1: Distorted monocapped trigonal prism coordination for bismuth oxide.

Two common bismuth-oxygen chains are known. The environment for the formation of $(BiO_2)^-$ chains is depicted in **figure 1.2.** [3]**.** A graphic representation of the very common $(Bi_2O_2)^{2+}$ sheets of the Aurivilluis phases can be found in **figure 1.3.** [4].

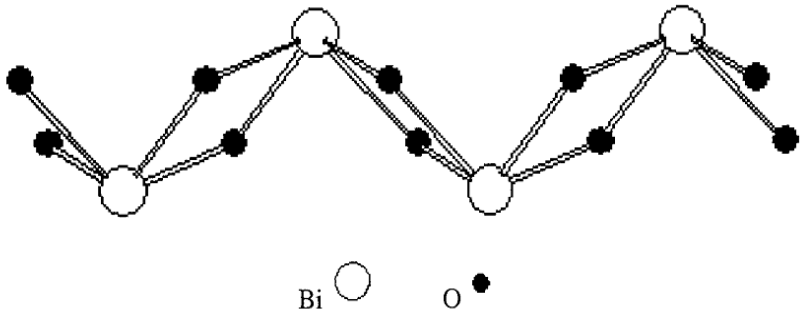

Figure 1.2: $(BiO_2)^-$ chain configuration for bismuth oxide.

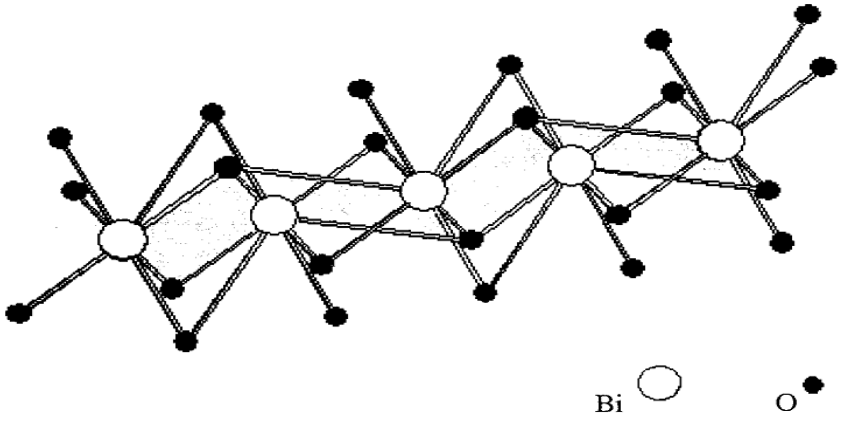

Figure.1.3: $(Bi_2O_2)^{2+}$ chain configuration for bismuth oxide.

Bi^{3+} compounds normally contain two, three or four short bonds that are never opposite one another. In $BiCu_2AsO_6$ an unusual five short bonds to bismuth is observed [5]. This highly unusual arrangement is depicted in **figure 1.4.** Hybridization of the 6s and 6p orbitals is required for lone pair stereochemistry. As covalency of the bonds increases, the lone pair influence on coordination tends to disappear [6]. Non-distorted polyhedrons are a result of this increase in covalency.

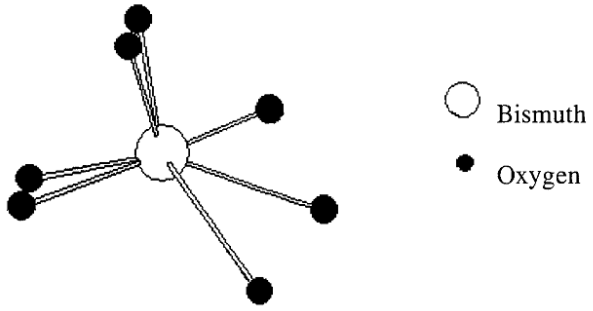

Figure 1.4: Unusual five short and two long coordination for bismuth oxide.

1.2.1 Properties of Bi_2O_3 system

1.2.1.1 Ferroelectric and Ferroelastic Properties

Ferroelectric materials contain oriented or aligned dipoles within the structure. Multiple domains with distinct directions dipole alignments are common. Applying an electric field to these materials can change the net polarization due to a shift in dipole direction orientation [7]. Materials exhibiting this behavior must be in a space group that lacks an inversion center and must contain a cation capable of undergoing significant displacement [8]. Many Aurivilluis phases, $Bi_2A_{n-1}B_nO_{3n+3}$ are ferroelectrics [9]. Ferroelastic materials contain a net spontaneous strain that is altered by applying a mechanical stress [10]. $BiVO_4$ undergoes a ferroelastic transition at 255°C that is associated with the monoclinic to tetragonal scheelite transformation [11]. It has been proposed that ferroelastic ability is intimately connected to displacement ability of Bi^{3+} cations due to the lone pair electron steric effect.

1.2.1.2 Conductivity

Many bismuth oxides are good oxygen ion conductors. This was first reported for δ-Bi_2O_3 [12]. The high oxygen ion conductivity has been explained by lone pair electron stereochemistry. The highly polarizable bismuth cation network can accommodate oxygen disordering within the structure and thus promote oxygen ion mobility [13]. Additional examples of oxygen ion conductors within the bismuth oxides include the entire $BiMeVO_x$ family [14], variants of $Bi_{23}M_4O_{44.5}$ where M can be phosphorus or vanadium [15].

Perhaps the most interesting type of conductivity among bismuth containing compounds is superconductivity. Two major categories of bismuth superconductors are currently known. One

set involves only Bi^{3+} cations, such as $Bi_2Cr_2Ca_3O_{10}$ [16]. In this and related superconductors, the bismuth stereochemistry do not plays active role in the expression of superconductivity. The second category of bismuth compounds exhibiting superconductivity are a mixed bismuth valent variety. In these systems superconductivity is associtated with the presence of both Bi^{3+} and Bi^{5+} [17]. Phases within the $Ba(Pb,Bi)O_3$ and $(Ba,K)BiO_3$ families are especially known for their superconductivity.

1.2.1.3 Optical Properties

Bi^{3+} is an attractive activator for luminescent materials. Its use has been widely studied and reported that the luminescence depends on the bismuth environment. UV emission is achieved from Bi^{3+} doped $LaGaO_3$ and Bi^{3+} doped La_2SO_2; while, red emission occurs for Bi^{3+} doped $BaSO_4$ and the compound $Bi_4Ge_3O_{12}$. $Bi_4Ge_3O_{12}$ is well established in luminescent applications. Bismuth oxyhalides have been investigated as light-sensitive layers for silver-free film development [18].

Some bismuth compounds exhibit nonlinear optics capabilities. These materials can produce a phase change or frequency conversion to laser light. Bi_2WO_6 was found to be a reasonably second harmonic generator and $BiCa_9V_7O_{28}$ has proven to be a second harmonic generator with three times the intensity of KH_2PO_4, one of the more common doubling crystals used today. Applications in the area of nonlinear optics include fiber optic communications, optical couplers, optical modulators and optical switches. The monoclinic phase of $BiVO_4$ has been examined by its bright yellow-orange color which makes it useful as a pigment.

1.3 Bismuth vanadate

The Bi_2O_3–V_2O_5 system has attracted much attention in recent years due to its unique properties such as ferroelasticity, dielectric, ionic conductivity and its potential applications in many scientific and technological fields. The most striking feature of this compound is its strong polar response, and high ionic mobility which gives a variety of applications in catalysts, gas sensors and solid-state electrolyte, as electrode materials for lithium rechargeable batteries and pyroelectric detectors. A number of phases have been identified in this binary system, including $BiVO_4$ [19,20], $Bi_4V_2O_{11}$ [21], $Bi_{3.5}V_{1.2}O_{8.25}$ [22], $Bi_{23}V_2O_{44.5}$ [23] and $Bi_8V_2O_{17}$ [24]. While much research has gone into the orthovanadate phases $BiVO_4$, particularly regarding its catalytic properties [25] and $Bi_4V_2O_{11}$ which is the parent compound of the BIMEVOX family of solid electrolytes [26].

1.3.1. Structural Aspects

The major goal is to synthesis new compounds with high oxygen ion conductivity at low temperature (400-800^{0}C). For synthesizing new conductors, attempts are made to combine the extrinsic vacancies through doping with the intrinsic vacancies already present in the structure, which creates the lattice distortion in the materials. This type of phenomena helps to generate the various types of structure as given below.

1.3.1.1. Fluorite Structure

Crystals of fluorite structure used in a number of fields of physics as well as technology of solid devices. Oxides which adopt the fluorite structure or structures related to fluorite have great and varied technological importance. Over the past decades, bismuth oxide (δ-Bi_2O_3) and doped Bi_2O_3 have been intensively studied for their high oxide ion conductivity because of these

reasons: (a) ¼ of the oxygen sites are vacant in the fluorite-type lattice (b) the electronic structure of Bi^{3+} is characterized by the presence of $6s^2$ lone pair electrons, leading to high polarizability of the cation network, which in turn leads to oxide ion mobility (c) the ability of Bi^{3+} to accommodate highly disordered surrounding.

The study of fluorite structured oxides as electrolytes begins with the early investigations by Walther Nernst in 1900; fluorite type, oxygen deficient structure of δ-Bi_2O_3 has been proposed by Sillén (1937) and Gattow (1962) [27]. The conductivity of bismuth oxide and mixed bismuth oxide has been first reported by Takahashi et al. [28]. The general formula of a fluorite oxide is AO_2. This structure is a face centered cubic arrangements of cations with anions occupying all the tetrahedral sites as shown in **figure 1.5.**

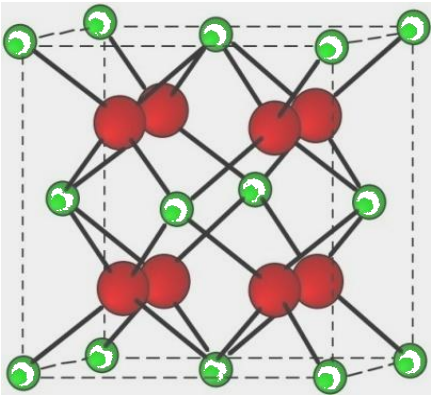

Figure 1.5. Unit cell for the fluorite (AO_2) structure.

(*green spheres represents the cation atoms and red spheres represents the anions atoms*)

The fluorite structure has a large number of octahedral interstitial voids. Oxide ion conduction is provided by oxide ion vacancies and interstitial oxide ions. Uranium dioxide (UO_2), thorium dioxide (ThO_2) and ceria (CeO_2) are the materials that readily form the fluorite structure. Additionally, the fluorite lattice pertains to many other compounds, such as halides (SrF_2), oxides (CeO_2) and intermetallics (NiMgBi).

1.3.1.2. Aurivillius Structure

Aurivillius structure was first reported by Aurivillius in 1949 [29, 30] and oxide ion conductivity was first reported by Takahashi and Yanovski in 1970. Abraham et al. [31] was published the first evidence of high oxide ion conductivity in $Bi_4V_2O_{11}$. The general formula of Aurivillius family, represented as $Bi_2A_{n-1}B_nO_{3n+3}$, it consists of n-perovskite [$A_{n-1}B_nO_{3n+1}]^{2-}$ layers sandwiched between bismuth oxide sheets $[Bi_2O_2]^{2+}$, where A represent 12-fold coordination and B represent the 6-fold coordination. Numerous dopants are able to substitute on the A and B sites (A = Na, K, Ca, Sr, Ba, Bi etc.; B = Fe, Cr, Ti, Ga, Nb, V, Mo, W etc.)[32] with restriction that the perovaskite layer and bismuth oxide layer must match to each other structurally [33]. Oxygen ion vacancies in the Perovskite layer leads to the high conductivity, Bi_2WO_6 or Bi_2MoO_6 (n=1) was the first member of the Aurivillius family [28].

The layered structure of $Bi_4V_2O_{11}$ undergoes several structural transitions between 405 ^{0}C and congruent melting point, 887 ^{0}C. Among the Aurivillius oxides, the $(Bi_2O_2)^{2+}$ $(VO_{3.5})^{2-}$ have a great attention due to its high conductivity [34]. The idealized structure of $Bi_4V_2O_{11}$ consist of $(Bi_2O_3)n^{2n+}$ and $(VO_{3.5}\square_{0.5})n^{2n-}$, where □ represents oxide ion vacancies as shown in **figure 1.6.** The Bi-O layer, exhibits Bi in a square pyramidal coordination. The asymmetric coordination geometry of Bi results from the stereo chemical activity of the non-bonding Bi $6s^2$ lone pairs. The V-O layer is composed of VO_6 octahedrons that contain oxygen vacancies to preserve electro neutrality. Thus, the V-O layer of ideal γ -phase can be described as $(VO_{3.5}\square_{.5})^{2-}$, where vanadium is pentavalent and □ denotes a randomly distributed oxygen vacancy. The β- and α-phases are characterized by the ordering of oxygen vacancies in the V-O layer. In the β-phases, the V-O layer still contains oxygen vacancies.

Generally speaking, three main phases are obtained in $Bi_4V_2O_{11}$ [29], at low temperature α-phase (below 445^0C) has low ionic conductivity, an intermediate temperature α-phase transforms to β-phase at 450^0C and at 570^0C temperature β-phase transforms to γ-phase. They emphasized the existence of a very high oxide ion conductivity in the γ-phase due to the disordering of the oxygen vacancies in the Vanadate $(VO_{3.5})^{2-}$ layers. The high conducting γ-phase of $Bi_4V_2O_{11}$ tried to stabilize at room temperature by adding the various types of dopants. Such types of substitutional solid compounds are known as BIMEVOX family.

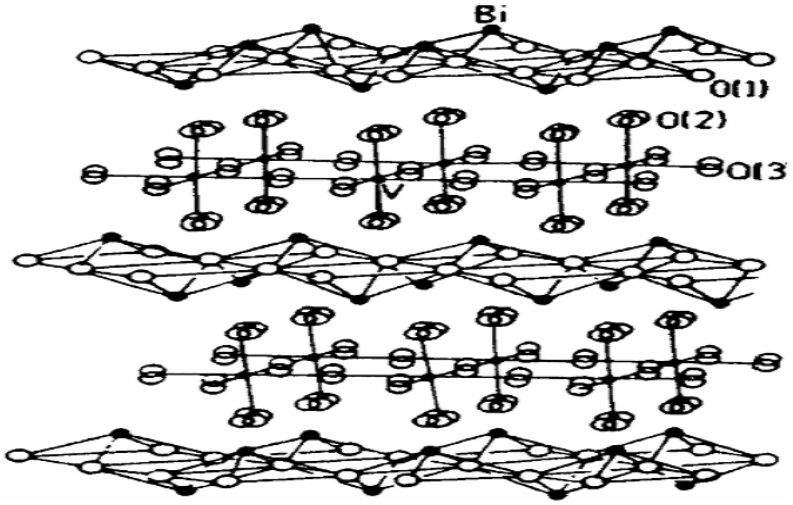

Figure 1.6. Aurivillius structure of bismuth vanadate.

1.3.2. Different crystalline phases

The compound $Bi_2VO_{5.5}$ and BIMEVOX have a characteristic layered structure and exhibit the three main polymorphs of α, β, and γ. However, besides α, β and γ phases, several phases that deviate from the three main phases are also exhibited. The crystalline structures of the three main phases are described by considering a subcell of $a_m = 0.55$, $b_m = 0.56$, and $c_m = 1.53$ nm. The α-phase is with reference to mean orthorhombic cell $a_m = 5.53$, $b_m = 5.61$, $c_m = 15.28$ A^o [6], for the ***β***- phase $a = b = a_m/2$, $c \approx c_m$; for the ***β***- phase $a_m \approx 2a_m$, $b_m = b_m$, $c_m \approx c_m$; for the **α**- phase

$a_m \approx 3a_m$, $b_m \approx b_m$, $c_m \approx c_m$ [7]. $Bi_2VO_{5.5-\delta}$ consists of alternate bismuth-oxygen (Bi-O) and vanadium-oxygen (V-O) layers.

The Bi-O layer formulated as $(Bi_2O_2)^{2+}$, exhibits Bi in a square pyramidal coordination. The asymmetric coordination geometry of Bi results from the stereo chemical activity of the non-bonding Bi $6s^2$ lone pairs. The V-O layer is composed of VO_6 octahedrons that contain oxygen vacancies to preserve electro neutrality. Thus, the V-O layer of ideal γ -phase can be described as $(VO_{3.5}\square_{.5})^{2-}$, where vanadium is pentavalent and $\square$ denotes a randomly distributed oxygen vacancy. The β- and α-phases are characterized by the ordering of oxygen vacancies in the V-O layer. In the β-phases, the V-O layer still contains oxygen vacancies. Besides α-, β-, and γ -phases several phases that deviate from the three main phases are observed.

The doped and undoped $Bi_4V_2O_{11}$ has been studied in wide range of substitution of various cations in different oxidation states such as Na^{2+}, Cu^{2+}, Ni^{2+}, Al^{3+}, Ga^{3+}, Ti^{4+}, Nb^{5+}, and W^{6+} for vanadium have been investigated in detail over the years[35]. $Bi_4V_2O_{11}$, well known for its oxide ion conductivity. $Bi_4V_2O_{11}$, normally represented as $Bi_4V_2O_{11}$ due to oxygen deiciency, was expected to show electronic conductivity at low temperatures. The experimental band gaps obtained from the UV–vis diffuse reflectance of different quenched and annealed samples were known to vary from 1.99 to 2.04 eV [35].

CHAPTER-2

LITERATURE REVIEW

New bismuth containing compounds in the Sleight group have been obtained through exploratory synthesis and through designed synthesis. In 1990, Huang and Sleight obtained and characterized the new compound $Nd_{1.7}Bi_{0.1}Sr_{0.9}Ca_{0.3}Cu_2O_6$ [36]. Despite containing CuO_2 sheets, this compound was determined to be non superconducting. Another property driven quest involved the oxyhalides. Oxyhalides tend to have interesting optical properties. BiOBr can luminesce with excitation from X-rays, UV light or cathode rays if doped with an appropriate rare earth activator. BiOCI has been investigated as the light-sensitive layer in photographic imaging. Two new bismuth containing oxychlorides were characterized, $BiSr_3O_3CI_3$ and $BiCa_3O_3CI_3$. Both are unique among bismuth oxyhalides in that the three-dimensional network contains oxygen and chlorine sites in one layer.

Huang and Sleight, synthesized two new compounds i.e. $BiSr_2V_3O_{11}$ and $BiBaV_3O_{11}$, containing two distinct vanadium groups, the orthovanadate group (VO_4) and the pyrovanadate group (V_2O_7). Phosphorus substitution for vanadium in the barium system provided the compound $BiBa_2V_2PO_{11}$ [6]. The phosphorus was found to have no preference for the ortho or pyro environments.

Characterization of $BiMg_2VO_6$ led to the systematic design of the isostructural compounds $BiMgPO_6$ and $BiMg_2VO_6$. Bi^{3+}, in a solid-state material, is simple to obtain. Bi^{5+} is more difficult due to instability. Bismuth mixed valent superconductors drove a design-oriented search for new materials within the alkali metal-bismuth oxide system. A collection of Bi^{5+} compounds

were developed using electro deposition and hydrothermal techniques. In 1998 a new family of rare earth bismuth oxynitrates was obtained from low temperature hydrothermal synthesis. Eight members of the $RBi_2O_4NO_3$,(R = Y, Sm, Eu, Gd, TB, Dy, Er, Yb,) were isolate and characterized. While looking for interesting ferroelectric and nonlinear optics properties within the BiA_2MO_6 (A = divalent cation, M= pentavalent cation) system, $BiCu_2AsO_6$ and $BiCuVO_6$ were discovered. $BiCu_2AsO_6$ contains unusually short bismuth to oxygen bond distances. $BiCuVO_6$ is different from other BiA_2MO_6 members because its VO_4 tetrahedron does not lie on any symmetry element. The tetrahedra do not point in directions along any of the unit cell axes.

Bismuth and calcium complex oxides have been of interest in the Sleight group since the discovery of $BiCa_9V_7O_{28}$ also by many groups. Huang and Sleight isolated $BiCa_4V_3O_{13}$ in 1993. In 1998 Radosovljevic, Evans and Sleight obtained $BiCa_2VO_6$. $BiCa_2AsO_6$ and $Bi_2CaV_2O_9$ [5] were characterized in 2000. $BiCa_4V_3O_{13}$, $BiCa_9V_7O_{28}$ and $Bi_2CaV_2O_9$ all contained disordered Bi/Ca sites and $BiCaVO_6$ and $BiCaAsO_6$ both generated second harmonic signals.

Two new bismuth cadmium vanadates $BiCdVO_5$ and $BiCd_2VO_6$ were discovered in 2000 [5]. Also $Bi_3Ca_9V_{11}O_{41}$ compound discovered in 2000 which contains three distinct vanadium environments. The third environment involves a pair of edge sharing VO_5 square pyramids each sharing a corner with a VO_4 tetrahedron, creating the unique V_4O_{14} polyhedron arrangement. This arrangement has never previously been reported. A second phase of $BiMgVO_6$ has also been determined and structurally characterized [5].

Pernot et al. studied that the partially Cu- or Ni-substituted compounds ($Bi_4V_{2(1-x)}M_{2x}O_{(11-3X)}$) ; (M=Cu,Ni) are highly oxygen conducting. Three phases are observed in the unsubstituted compound i.e. α, β and γ phases at room temperature 400 and 550 ^{0}C, respectively. Structure are

studied as a function of substitution on the vanadium sites between 0 and 6 mol% at room temperature and the Cu compound remains in the orthorhombic α-phase.

Yan et al. prepared $Bi_4V_{2-x}M_xO_{11-x/2}$ (M=Ti, Zr, Sn, Pb) by solid state reactions. They observed that all the substituted phases retain the α-phase for $x<0.20$. In the $Bi_{4-x}Me_xV_2O_{11-\delta}$ system, substitution on V as well as Bi site is possible. Since it is presumed that the oxygen vacancies are present in perovskite vanadium layers; so substitution on bismuth sites is assumed to have very less effect on the ionic conductivity. These vacancies can be increased after doping of aliovalent cations. The substitution of Pb^{2+} on bismuth site may likely to compensate the charge in the Bi_2O_2 layers leading to additional oxide vacancies for $x \leq 0.2$.

As in BVO, vanadium could exist mostly in two stable states, i.e.V^{4+} and V^{5+}. So, this leads to the large amount of oxygen ion vacancy formation. This internal structure does affect the optical properties of fabricated thin films.

According to Yang et al. [37] the crystal structure changes with Mn doping, so the change in optical constants and band gap is also expected. Moreover there might be intrinsic reasons like structural and microstructural change, strain and disordering due to Mn doping affecting the optical properties of these films.

The compound of $Bi_2V_{1-x}Nb_xO_{5.5}(0\leq x\geq 0.4)$ thin films have been successfully fabricated on $Pt/TiO_2/SiO_2/Si$ and corning glass substrates using pulsed laser deposition technique and studied their structural, optical and dielectric properties by Kumari et al. [38]. According to them fabricated films exhibited layered perovskite structure with no preferred orientation unlike in the case of undoped BVO. The band gap of Nb doped BVO films increased slightly with the increase

in Nb content and was attributed to a decrease in number of oxygen ion vacancies. The refractive index of BVN thin films was found to increase with increasing Nb.

Kohtani et al. [39] prepared Cu-$BiVO_4$ catalyst by impregnation method from aqueous solution of $Cu(NO_3)_2.3H_2O$. The Cu-$BiVO_4$ series catalysts showed the absorption in the visible region between 550 and 800 nm and the absorption intensity increased with the increase of Cu content and also found that Cu loading could effectively narrow down the band-gap of the catalysts.

Yan Bing and Li lingzhi [40] prepared $La_{0.3}Bi_{0.7}VO_4$ by hydrothermal method in 2008. The characteristic patterns of XRD, TEM, SEM and UV-Vis-DRS showed that the $La_{0.3}Bi_{0.7}VO_4$ and Bi_2O_3 had better crystallization, smaller crystal size, and stronger response to visible light. They reported that the absorption band threshold of $La_{0.3}Bi_{0.7}VO_4$ and Bi_2O_3 reached at 480 nm and 533 nm, and the band gap energies were estimated to be 2.58 eV and 2.33 eV, respectively. Luo Hongmei et al. [41] fabricated the monoclinic scheelite $BiVO_4$ films by polymer-assisted deposition technique. Changes in the processing conditions of the films result in different absorption spectra of $BiVO_4$. The lack of an absorption band at around 400- 500 nm of $BiVO_4$ in the UV-Vis spectra results in no detectable photocurrent. In samples where the absorption band was present, a photocurrent was also observed.

Xu Hui et al. [42] synthesized Cu-$BiVO_4$ series catalysts by impregnation method in 2008. According to them, the series of Cu-$BiVO_4$ catalysts showed the absorption in the visible region between 550 and 800 nm. The absorption intensity increased with increasing the content of copper and also they observed that the copper doping could effectively narrow down the band-gap of the catalysts. The copper contained samples display the higher photocatalytic activities as compared to the pure $BiVO_4$ and the highest photodegradation efficiency of methylene blue was

obtained. The results of XPS and SEM indicated that Cu, CuO was dispersed on the surface of $BiVO_4$.

Kumari et al. [38] studied the thin film of $Bi_2V_{1-x}Nb_xO_{5.5}$ ($0 \leq x \geq 0.4$). This compound was fabricated by pulsed laser deposition on platinized silion substrates and the compound was studied under the UV-Visible spectra by using spectroscopic ellipsometry. The band gap of Nb doped BVO thin films was slightly higher (3.13 eV for x = 0.4) than undoped (2.91 eV) films and was attributed to a decrease in number of oxygen ion vacancies. By using the same technique for the preparation of specimens, Kumari et al. studied the optical properties of Mn doped Bismuth Vanadate ($Bi_2V_{1-x}Mn_xO_{5.5-x}$ where x = 0.05, 0.1, 0.15 and 0.2%) thin films. The band gap energy for undoped films was 2.2 eV [43].

The observed optical band gap increases from 2.52 to 2.77 eV, if the concentration of Mn increases from x = 0.05 to x = 0.15 and then decreased to 2.7 eV for the more concentration of Mn. That means the number of oxygen vacancies increased in BVM films due to increased band gap. On the contrary the decreased optical band gap for BVM film with x = 0.2 might be due to the more distortion created.

Deepti et al. [44] fabricated the $Bi_{4-x}M_xV_2O_{11}$ (M = La, Gd, $0 \leq x \geq 0.4$) by solid state reactions. According to the XRD pattern the first three composition in both the system exhibited α- phase with some extra peaks particularly in x = 0.2 and x = 0.3 samples and also some peak broadening or peak shifting were observed in these samples. XRD peak broadening and shifting in the substituted samples has been attributed mainly to the disordering and strain introduced through La^{3+} and Gd^{3+} doping for Bi^{3+} in parent sample and α to β-phase transition at lower side of the temperature. The high temperature β-phase of $Bi_4V_2O_{11}$ is stabilized for $Bi_{4-x}M_xV_2O_{11}$ with M = Gd, La and $x \geq 0.4$.

Zhang et al. [45] synthesized a pure phase monoclinic bismuth vanadate powders of a nanosized diameter were by hydrothermal method and these samples were characterizied by XRD, TEM, DRS, Raman and FTIR techniques. In the case of FTIR, they found that all the samples are mainly characterized by a broad and strong IR band near 728 cm^{-1} with shoulders at 892, 822, 684 and 632 cm^{-1} and also a weak CO_3^- derived band is observed at 1386 cm^{-1} due to the absorption of atmospheric carbon dioxide during the experiments. It reveals that all the samples exhibited the same monoclinic scheelite structure, although their particle diameters and particle morphologies increased in a continuous manner as the hydrothermal temperature increased from 140 to 240 ^{0}C.

A composite catalyst Gd_2O_3/ $BiVO_4$ prepared with hydrothermal method in 2010 by Zhang et al. [46]. According to them, all the composite photocatalyst showed a structure of monoclinic $BiVO_4$ type and dispersed particles with high crystallinity than pure $BiVO_4$, which enhanced the photocatalytic activity when decomposed Methyl Orange molecules in aqueous solution under visible light irradiation.

Bismuth Vanadates ($BiVO_4$) with various crystal structures (tetragonal zircon, monoclinic scheelite, and tetragonal scheelite) and morphologies (sphere, nanosheet, dentrite, and flower-like) were fabricated with a mild additive-free hydrothermal method under different preparation conditions. Guo Yingna et al. [47] found that these $BiVO_4$ samples possess different photophysical and photocatalytic properties. Among all the tested powders monoclinic scheelite $BiVO_4$ with a flower like morphology showed the highest UV-Visible photocatalytic reactivity towards dyes RB and MB degradation.

With hydrothermal technique, a pure nano crystalline $BiVO_4$ was prepared and the band gap was 2.45 eV and 2.40 eV at the wavelength 523 and 540 nm respectively. In 2010 a tetragonal $BiVO_4$

nanoparticle were synthesized by Osrio A. Fernandez et al.[48] using coprecipitation method. According to them, the tetragonal and monoclinic samples present a broad absorption band between 250 to 650 nm, with a maximum absorbance around 410 nm. Optically bands intensely absorb the blue light (400-500 nm) resulting in highly saturated yellow shades so that tetragonal $BiVO_4$ was orange-yellow which monoclinic $BiVO_4$ was canary yellow.

Dragomir and valant were synthesized the Nd-doped $BiVO_4$ and Bi- doped $NdVO_4$ compound by solid state method [49]. They studied the structural and optical peoperties of the samples with various techniques. The X-ray powder diffraction technique was used for the phase composition and crystallographic details and the band gaps were determined from UV-Visible diffuse reflectance spectroscopy.

Kaur et al.[50] fabricated the $Bi_4V_{2-x}M_xO_{11-\delta}$ ($0 \leq x \leq 0.4$ x in one step 0.1, M = Mn, Ga, As,) by solid state reactions. All samples show the single phase and their band gap lies from 1.824 to 2.13 eV respectively. $Bi_4V_{1.8}M_{0.2}O_{11-\delta}$ shows the highest conductivity due to low band gap value.

Thakral et al.[35] studied the photocatalytic properties of $Bi_4V_2O_{11-\delta}$. Other bismuth based compound such as Bi_2GaVO_7, Bi_2YVO_8, and Bi_2AlVO_7 were also reinvestigated. They observed band gap of 2.14 eV for Bi_2GaVO_7 and also appropriate shift in the band gap was noticed for $Bi_2V_{1.6}Ga_{0.4}O_{11-}$ (2.03eV) as compared to $Bi_4V_2O_{11-\delta}$.

Based on literature review on doped and undoped bismuth vanadate can be concluded that the optical band gap is very sensitive to processing conditions and chemical nature of dopant. Some times, the doping concentration leads to the formation of secondary phases. The formations of secondary phase markedly affect the optical properties of these systems. Additionally the dopants site also plays very important role to decide the properties of these materials.

CHAPTER 3

EXPERIMENTAL TECHNIQUES AND MEASUREMENT

The aim of the present work is to study the structural and optical properties of the specimen by using X-ray diffraction analysis, Fourier transform infrared spectroscopy (FTIR), UV-Visible spectroscopy, Scanning electron microscopy (SEM) and energy dispersive spectroscopy (EDS) techniques. The details of these techniques are given below.

3.1. Sample preparation

The $Bi_{4-x}M_xV_2O_{11}$ (M = La, Gd; $0 \leq x \geq 0.4$) powders synthesized by solid state reaction technique taking stoichiometric amounts of the Bi_2O_3, V_2O_5, La_2O_3, Gd_2O_3 oxides. The mixture of starting powders was ball-milled using porcelain milling jar for 2 hours in acetone media after manually mixing in mortar pestle for half an hour.

The resulting mixture was dried, thoroughly ground to break up any large agglomerates, and then heat treated at 700^0C in silica crucible for 12 hours. To ensure complete reaction the materials again ground and heat treated at 800 ^{0}C in a silica crucible for 12 hours. Disc shaped pellets were formed by uniaxially cold pressing 6gm powder of $Bi_{4-x}M_xV_2O_{11}$ (M = La, Gd) applying pressure of approximately 11 kN/m^2. The approximate pellets dimensions were 20 mm diameter by 3 mm thickness. The disc shaped pellets were sintered at 800 ^{0}C for 10 hours followed by furnace cooling.

3.2. Characterization

The samples are characterized by using X-ray diffraction (XRD), Scanning electron microscope (SEM), Fourier Transform Infrared Spectroscopy (FTIR), and Ultraviolet-visible spectroscopy (UV). The technical details of characterization techniques are given below.

3.2.1. X-ray diffraction

XRD is a non distributive technique that reveals information about chemical composition and crystallographic structure of materials. The XRD pattern of a pure substance is, therefore, like a fingerprint of the substance. When an X-ray beam hits an atom, the electrons around the atom start to oscillate with the same frequency as the incoming beam. Almost in all directions we will have destructive interference, that is, the combining waves are out of phase and there is no resultant energy leaving the solid sample.

However the atoms in a crystal are arranged in a regular pattern, and in a very few directions we will have constructive interference. The waves will be in phase and there will be well defined X-ray beams leaving the sample at various directions. Hence, a diffracted beam may be described as a beam composed of a large number of scattered rays mutually reinforcing one another.

According to Bragg's law, when a beam of X-rays of wavelength λ enters a crystal, the maximum intensity of the reflected ray occurs when $\sin\theta = n\lambda/2d$, where θ is the complement of the angle of incidence, n is a whole number, and d is the distance between layers of atoms. X-ray powder diffractions study was performed at room temperature using PANalytical X'Pert PRO system with Ni-filter in the range of $10^{\circ} \leq 2\theta \geq 80^{\circ}$ with step size of 0.013°/min. The XRD data was matched with ICDD to confirm the phases formed in samples. Illustration of the Bragg's law as shown below:

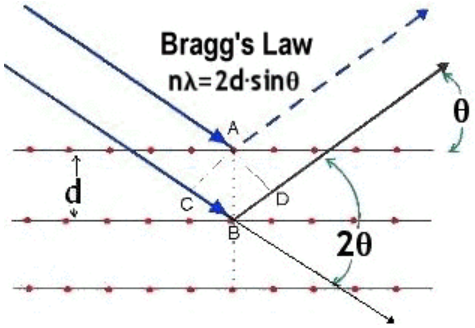

Figure 3.1: Illustration of the Bragg's law.

3.2.2. Fourier Transform Infrared Spectroscopy (FTIR)

FTIR is the most powerful tool for identifying types of chemical bonds, and unknown materials. It can be used to identify chemicals from spills, paints, polymers, coatings, drugs, and contaminants. It can be applied to the analysis of solids, liquids, and gasses. It can also determine the quality of sample and the amount of components in a mixture.

The principle of FTIR is based on the fact that bonds and groups of bonds vibrate at characteristic frequencies. A molecule that is exposed to infrared rays absorbs infrared energy at frequencies which are characteristic to that molecule. In a molecule, the differences of charges in the electric fields of its atoms produce the dipole moment of the molecule. Molecules with a dipole moment allow infrared photons to interact with the molecule causing excitation to higher vibrational states. Diatomic molecules do not have a dipole moment since the electric fields of their atoms are equal. During FTIR analysis, a spot on the specimen is subjected to a modulated IR beam.

The specimen's transmittance and reflectance of the infrared rays at different frequencies is translated into an IR absorption plot consisting of reverse peaks. The resulting FTIR spectral pattern is then analyzed and matched with known signatures of identified materials in

the FTIR library. The FTIR of $Bi_{4-x}\ M_xV_2O_{11}$ (M=La, Gd and $0.1 \leq x \leq 0.4$) was recorded at room temperature in the range 450 to 4000 cm^{-1}. The instrumental picture of FTIR as shown below:

Figure 3.2: Set up of FTIR.

3.2.3. Scanning Electron Microscope (SEM)

Scanning electron microscopy is a most powerful tool for checking the crack surfaces, phase distribution, compositional differences and crystal orientation. The first Scanning Electron Microscope (SEM) debuted in 1942 with the first commercial instruments around 1965. Scanning electron microscope uses a focused beam of high-energy electrons to produce a variety of signals at the surface of solid specimens. The signals that derive from electron sample interactions reveal information about the sample including external morphology, chemical composition and crystalline structure and orientation of the materials make up the sample. data are collected over a selected area of sample and **α**-dimensional image is generated.

The SEM can also be used to study the chemical composition of sample using the energy dispersive spectroscopy. In SEM, accelerated electrons carry significant amount of kinetic energy and this energy is dissipated as a variety of signals produced be electrons- sample interactions when incident electrons are decelerated in the solid sample. These signals include

secondary i.e., Backscattered electrons. Diffracted Backscattered electrons that are used to analyze the morphology of sample.

The morphology and microanalysis of the samples were carried out on gold sputtered fractured surfaces of pellets by scanning electron (JSM-6510LV, JEOL and EDS). The instrumental picture of scanning electron microscope as shown below:

Figure 3.3: Apparatus of scanning electron microscope.

3.3.4. Ultraviolet and Visible Spectroscopy

Optical measurements constitute the most important means of determining the band structures of semiconductor. Ultraviolet-visible (UV-Vis) spectroscopy is one of the more ubiquitous analytical and characterization techniques in science. There is a linear relationship between absorbance and absorber concentration, which makes UV-Vis spectroscopy especially attractive for making quantitative measurements. In many applications other techniques could be employed but none rival UV-Visible spectroscopy for its simplicity, versatility, speed, accuracy and cost-effectiveness. UV Visible spectrophotometer measures the response of a sample to ultraviolet

and visible range of electromagnetic radiations. Molecules and atoms have electronic transitions while most of the solids have inter band transitions in the UV and Visible range. Therefore energy band gap can be calculated by measuring the absorption of coefficients of molecules. Let the photon beam intensity I_O is incident on the sample of the thickness t and I_t is the intensity of transmitted light then ,

$$I_t = I_O e^{-\alpha t} \quad \text{---------- (1)}$$

Band gap of the samples calculated by using the following relation

$$\alpha h\nu = A (h\nu - E_g)^n \quad \text{---------- (2)}$$

Where α is the absorption coefficient, h is planck's constant, ν is frequency, E_g is optical band gap and n is a constant associated to different types of electronic transitions n = ½, 2, 3/2 or 3 for direct allowed, indirect allowed, direct forbidden, and indirect forbidden transitions. The instrumental set up of UV-Vis spectrophotometer (model: Hitachi U-3900H) at room temperature has been used for our work as shown below:

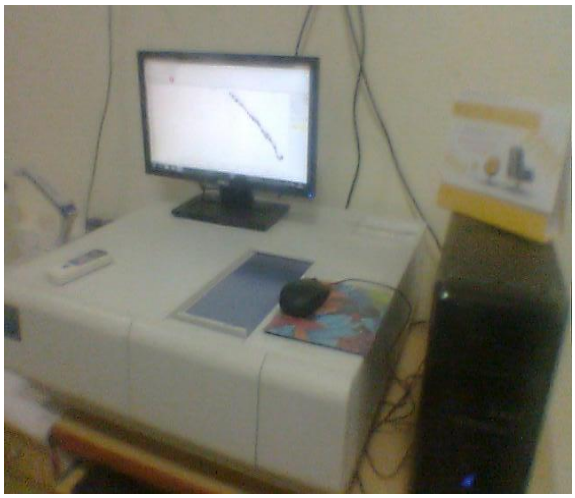

Figure 3.4: Set up of UV-Vis spectroscopy.

CHAPTER 4

RESULTS AND DISCUSSION

The samples were synthesized by solid state reaction method. These samples were characterized by different techniques. The obtained results are discussed in this chapter.

4.1. Crystal Structure

The X-ray diffraction pattern of $Bi_{4-x}La_xV_2O_{11}$ and $Bi_{4-x}Gd_xV_2O_{11}$ are shown in **figure (4.1, 4.2).** XRD results shows the doublets characteristics peaks at $2\theta \approx 31^0$, 39^0, 48^0, 54^0 and a very weak reflection at $2\theta \approx 24.2^0$. The weak reflection is attributed to the superstructure of α-$Bi_4V_2O_{11}$ [31]. Excluding the weak reflection, all the observed reflections indexed as an orthorhombic unit cell and this unit cell considered as the basis cell of the α-$Bi_4V_2O_{11}$. The structure of $Bi_4V_2O_{11}$ is monoclinic has reported by Joubert et al.[51], which is closely related to the earlier reported orthorhombic lattice. The monoclinic pattern has the doublet characteristics between $2\theta \approx 45.5$ and 46.5^0 which is a singlet in the orthorhombic pattern.

The recorded XRD spectra of $Bi_{4-x}Gd_xV_2O_{11}$ and $Bi_{4-x}La_xV_2O_{11}$ with x = 0.1, 0.2, and 0.3 could be indexed with α- $Bi_4V_2O_{11}$ [51] with lattice parameters comparable to the reported ones. It revealed that the first three compositions, in both cases have α-phases. Except x = 0.1, $Bi_{4-x}La_xV_2O_{11}$ has Bi_2O_3 as secondary phase. For Gd doped samples, Gd_2O_3 and Bi_2O_3 are present as impurity. It can be seen from the XRD patterns that with impurity concentration, the peak width increases and intensity of the XRD peaks decrease as shown in **figure 4.2.** For the

impurity concentration (x = 0.4) the α- phase is converting into β- phase as there is a shifting of peak to the lower 2θ. It could be indexed as β- $Bi_4V_2O_{11}$.

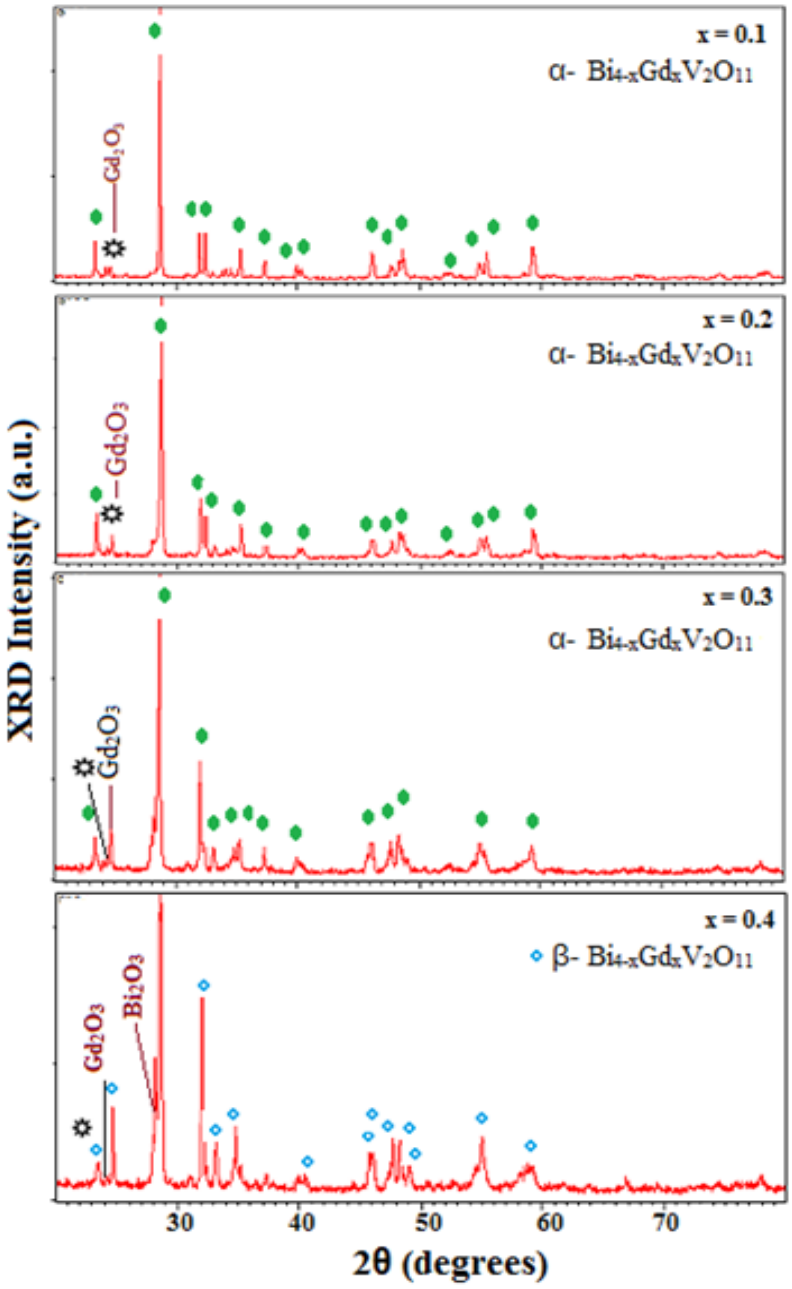

Figure 4.1: X- ray spectra of $Bi_{4-x}Gd_xV_2O_{11}$ (0≤x≥0.4); (✡) supperlattice reflection.

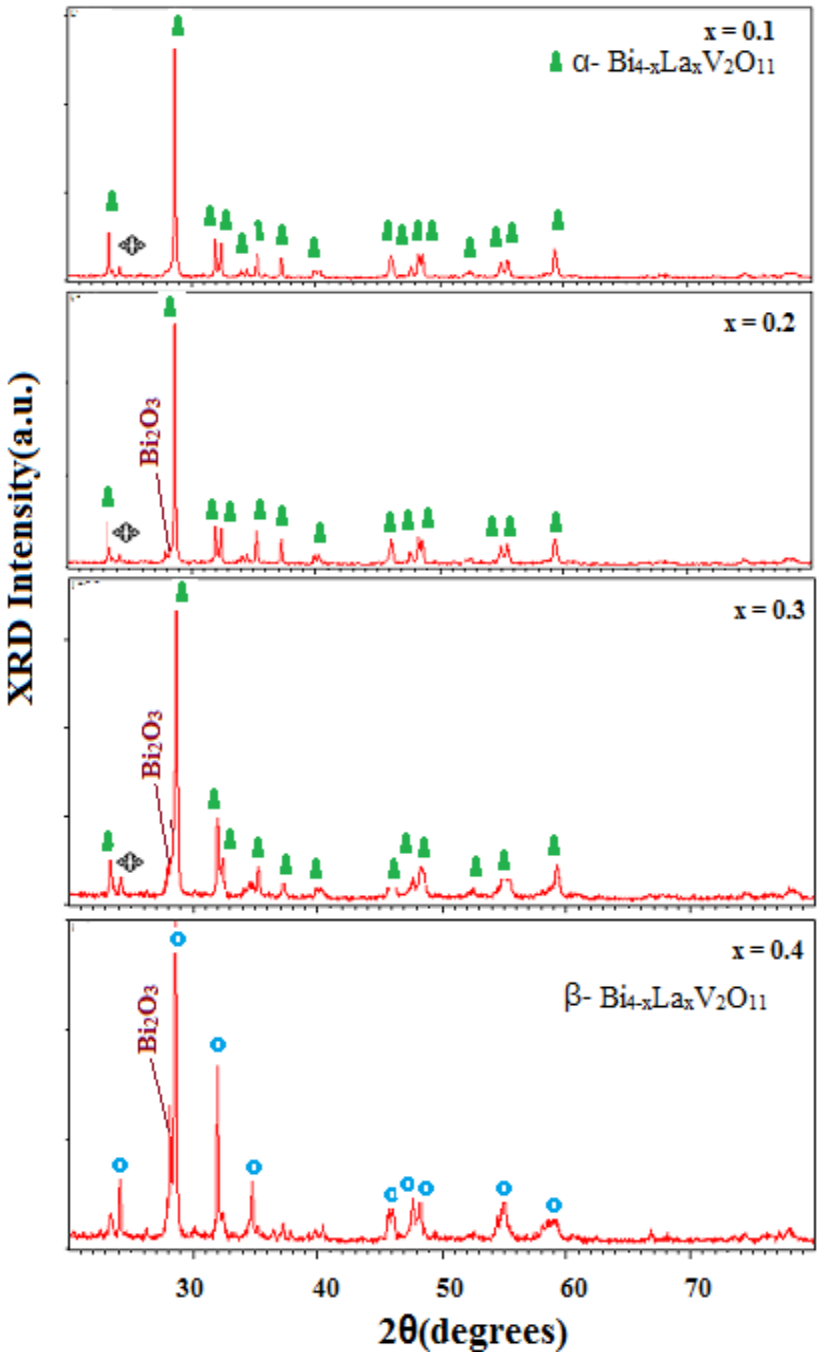

Figure 4.2: X- ray spectra of $Bi_{4-x}La_xV_2O_{11}$ ($0 \leq x \geq 0.4$) ; (✲) supperlattice reflection.

The lattice parameters of all the samples are tabulated in **table 1** and variation of lattice parameters with concentration for all the samples are shown in **figure (4.3, 4.4)**. For $Bi_{4-x}Gd_xV_2O_{11}$, a, b and c lattice parameters remains almost constant up to x=0.2 and after that a

decreases, b and c increases. The overall volume of the unite cell also remains constant upto x=0.2 and after that decreases. From the variation of lattice parameters it can be concluded that for Gd doped $Bi_4V_2O_{11}$ solid solubility lies at $x \geq 0.2$. For $Bi_{4-x}La_xV_2O_{11}$, the lattice parameter a decreases upto x=0.2 and after that increases for x=0.3, while b and c increases upto x=0.3. The overall cell unit volume also decreses uto x=0.2 and again increases for x=0.3. it can be concluded that solid solubility limit for the La doped samples lies upto $x \leq 0.1$. The Gd and La doped $Bi_4V_2O_{11}$ samples show difference in variation of lattuce parameters and unit cell volume. This may be due to the difference in ionic radii of La (1.032 Å) and Gd (0.938 Å). The graphical and tabular representation of the lattice parameters as shown below:

Table 1: Lattice parameters of $Bi_{4-x}Gd_xV_2O_{11}$ and $Bi_{4-x}La_xV_2O_{11}$ ($0.1 \leq x \geq 0.4$).

Sample Name	Composition	a(Å)	b(Å)	c(Å)	Volume(Å)^3
$Bi_{4-x}Gd_xV_2O_{11}$	**x = 0.1**	5.61	15.23	16.60	1419.70
	x = 0.2	5.61	15.23	16.60	1419.70
	x = 0.3	5.47	15.28	16.94	1418.35
	x = 0.4	5.59	15.29	5.53	473.53
$Bi_{4-x}La_xV_2O_{11}$	**x = 0.1**	5.58	15.28	16.60	1417.77
	x = 0.2	5.58	15.28	16.60	1417.70
	x = 0.3	5.61	15.28	16.53	1417.77
	x = 0.4	5.59	15.29	5.53	473.53

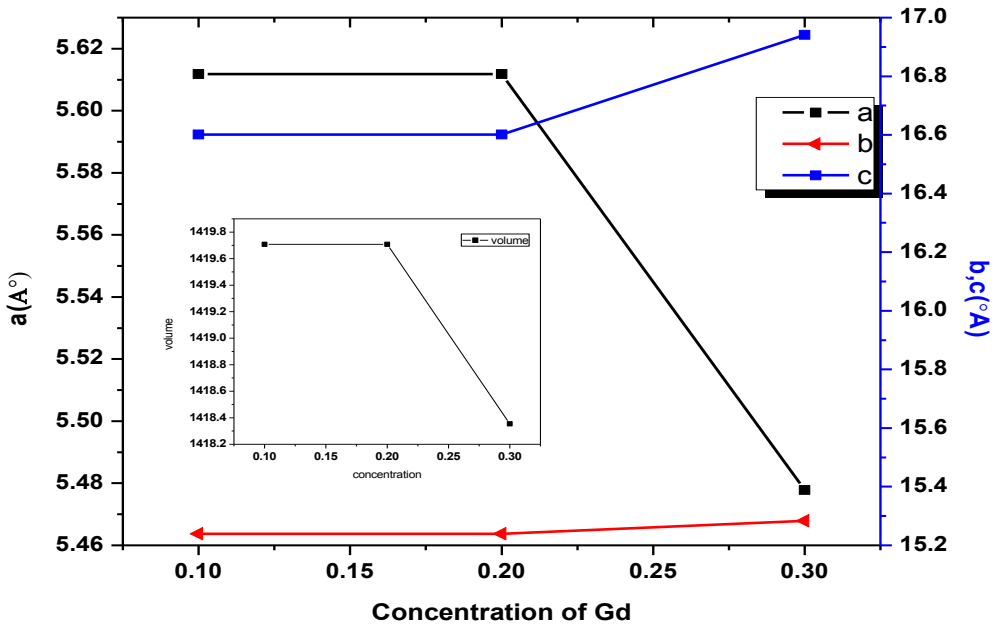

Figure 4.3: variation of lattice parameters & volume with conc. of Gd, $Bi_{4-x}Gd_xV_2O_{11}$ ($0 \leq x \geq 0.4$).

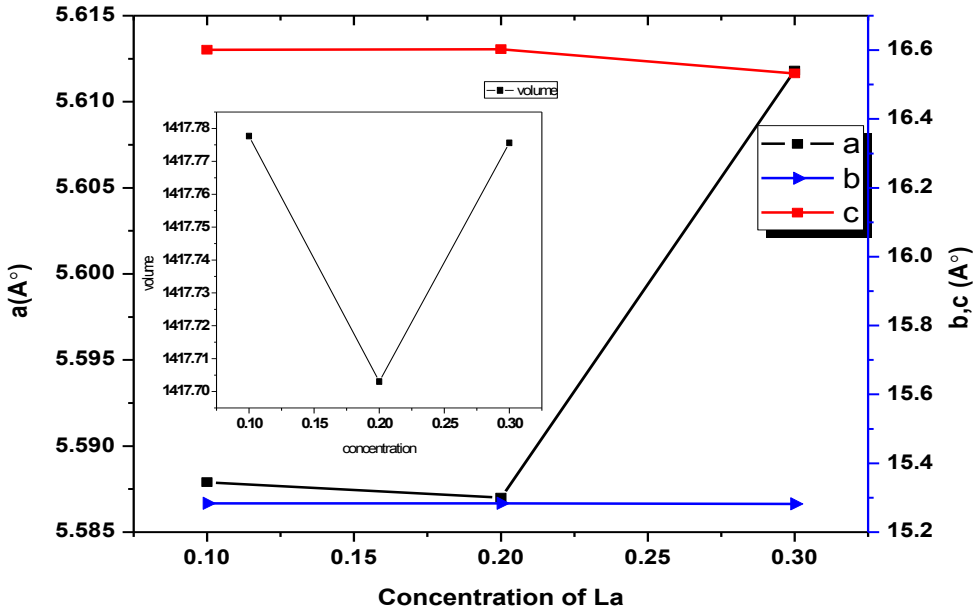

Figure 4.4: variation of lattice parameters &volume with conc. of La, $Bi_{4-x}La_xV_2O_{11}$ ($0 \leq x \geq 0.4$).

4.1.2. Scanning electron microscope and energy dispersive analysis

The SEM micrographs of fractured surface and energy dispersive analysis of the $Bi_{3.9}Gd_{0.1}V_2O_{11}$, $Bi_{3.7}Gd_{0.3}V_2O_{11}$ and $Bi_{3.9}La_{0.1}V_2O_{11}$ and $Bi_{3.7}La_{0.3}V_2O_{11}$ are shown in **figure 4.5.**

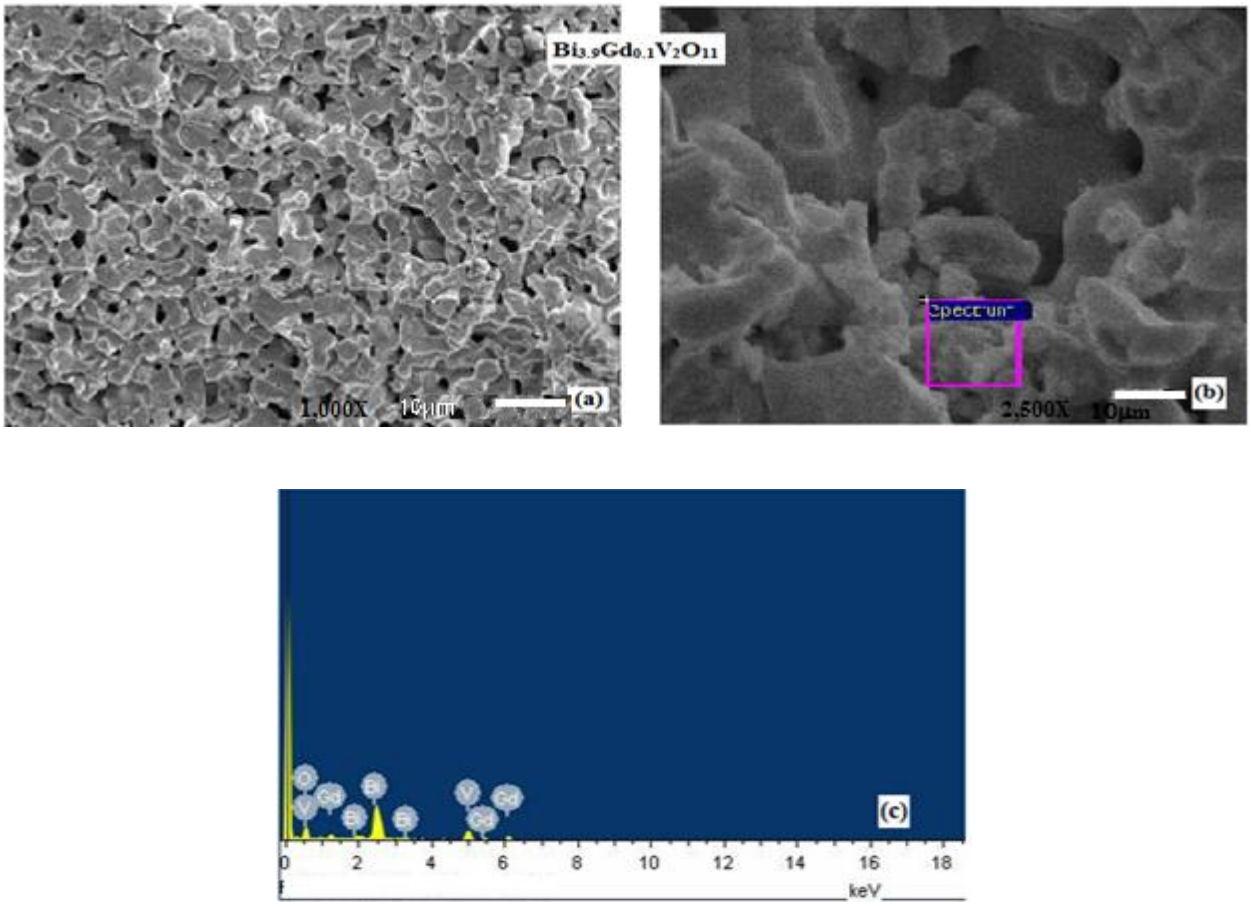

Figure 4.5: (a) & (b) SEM micrograph and (c) EDS, of $Bi_{3.9}Gd_{0.1}V_2O_{11}$.

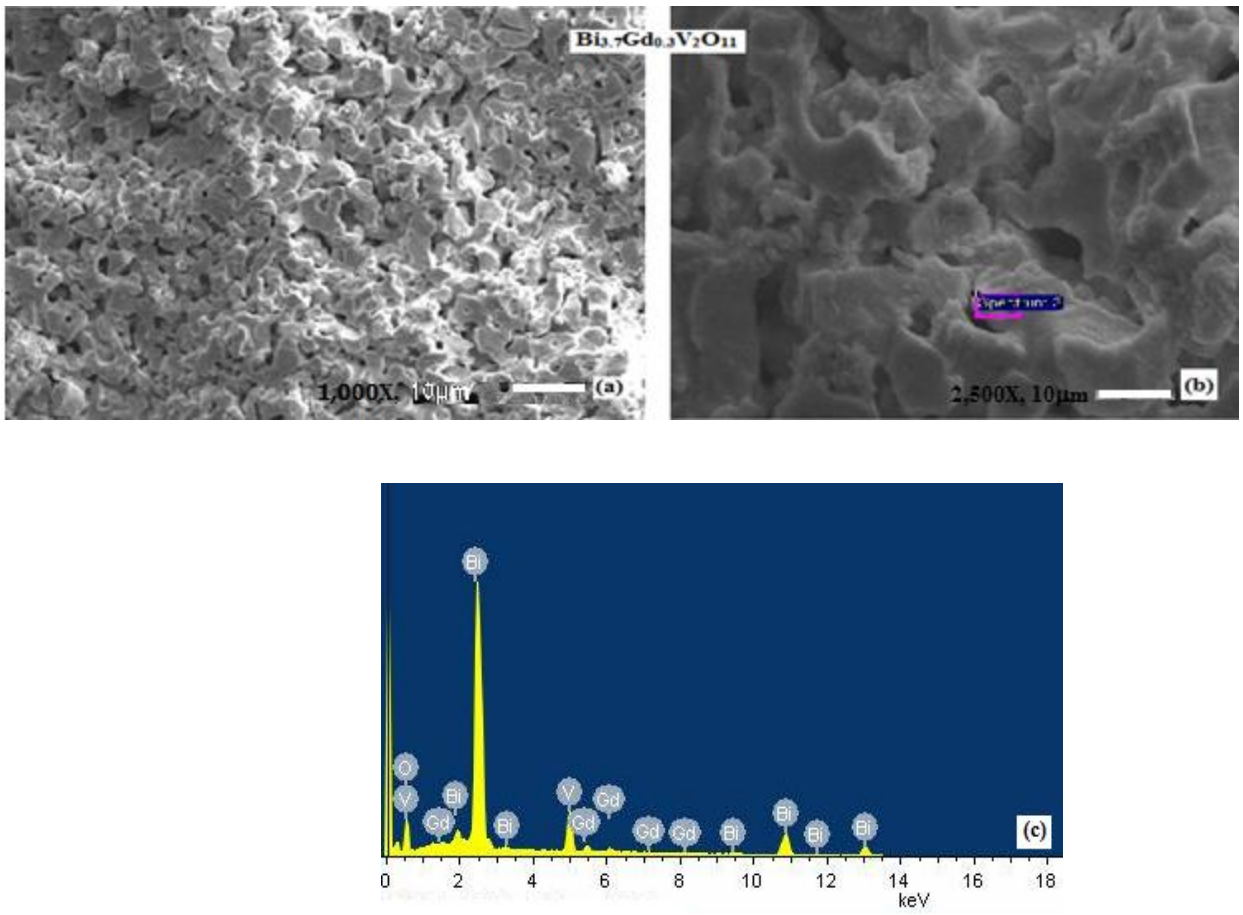

Figure 4.6: (a) & (b) SEM micrograph and (c) EDS, of $Bi_{3.7}Gd_{0.3}V_2O_{11}$.

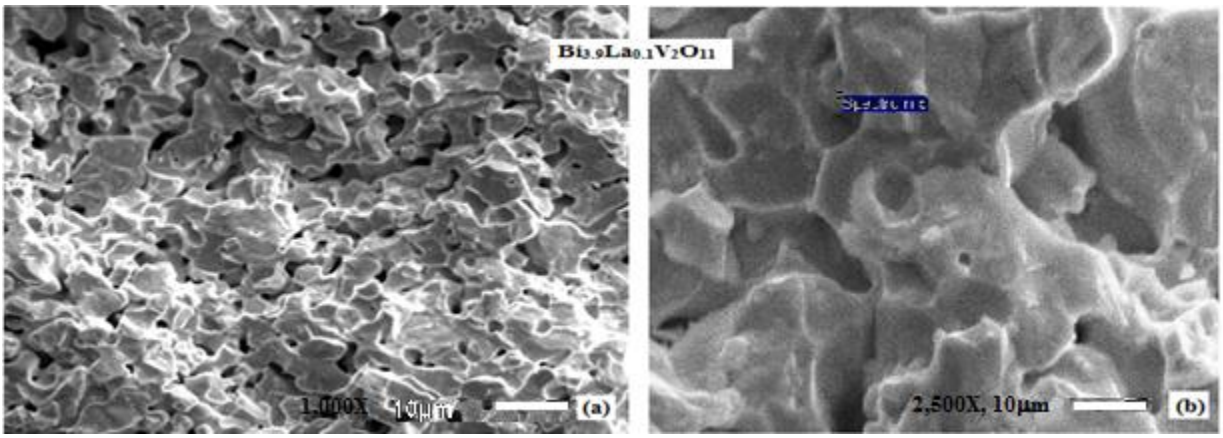

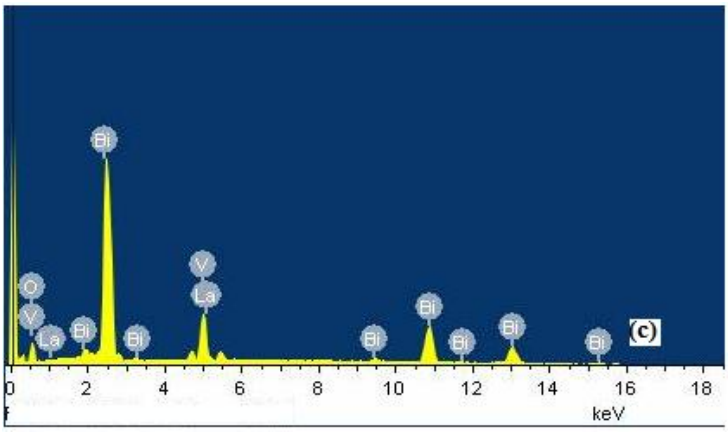

Figure 4.7: (a) & (b) SEM micrograph and (c) EDS of $Bi_{3.9}La_{0.1}V_2O_{11}$.

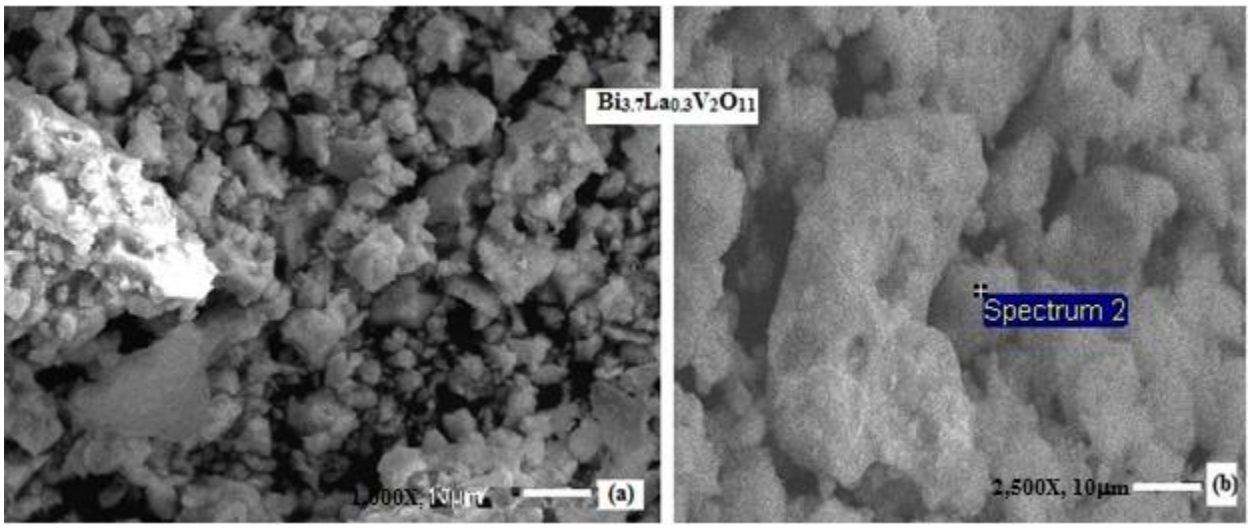

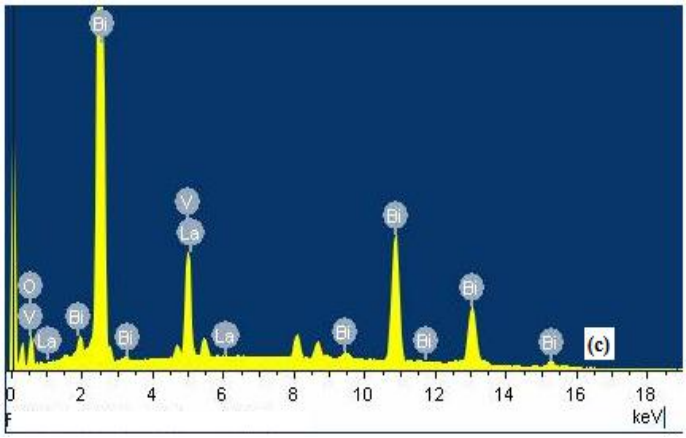

Figure 4.8: (a) & (b) SEM micrograph and (c) EDS, of $Bi_{3.7}La_{0.3}V_2O_{11}$.

We observed the secondary phase of the sample through XRD as well as SEM. The secondary phase might be Bi_2O_3, La_2O_3 and Gd_2O_3. Also we observed the grain size of the samples by SEM, and the grain size varies in the range of 3 to 7 μm. It is cleary observed that the grains are non- uniform in all the samples. All the samples show the continual and closed pores. As concentration of the dopant increases the porocity and grain size marginally decreases as shown in **figure 4.6(a)**.

In contrast to this, the doping of La^{3+} in samples leads to increase the porosity with larger grain size as observed in **figure 4.7(a) & (b).** All four examined samples show the typical characteristics as observed in many ceramic samples [52]. In all the samples, the EDS analysis is also performed. The elemental compositions of the samples were determined by the energy dispersive spectroscopy as given in **table 2**. The qualitative analysis support the XRD results.

Table 2: The atomic percentage of $Bi_{4-x}M_xV_2O_{11}$ (M=La, Gd at x=0.1, 0.3).

Elements (In shell)	**Atomic %**			
	$Bi_{3.9}Gd_{0.1}V_2O_{11}$	**$Bi_{3.7}Gd_{0.3}V_2O_{11}$**	**$Bi_{3.9}La_{0.1}V_2O_{11}$**	**$Bi_{3.7}La_{0.3}V_2O_{11}$**
Bismuth (M)	10.97	22.01	23.08	30.58
Gadolinium(L)	2.66	1.00	-	-
Lanthanum (L)	-	-	3.16	2.56
Oxygen (K)	77.48	66.39	57.21	46.19
Vanadium (K)	8.89	10.60	16.55	20.67

4.1.3. Fourier Transform Infrared Spectroscopy (FTIR)

The FTIR spectra of recorded $Bi_{4-x}Gd_xV_2O_{11}$ and $Bi_{4-x}La_xV_2O_{11}$ ($0 \leq x \geq 0.4$) samples, ranging from 400 to 1800 cm^{-1} are shown in **figure (4.9, 4.10)** respectively. The vibrational bands observed in the range of 610 to 620 cm^{-1} and 480 to 495 cm^{-1} in all the samples can be assigned to Bi- O- Bi stretching vibrations in BiO_6 octahedral units [53]. The bands at 720, 780, 928 cm^{-1} can be due to the V-O-V stretching. Apart from these bands, a very weak band is also observed in **figure 4.9** which is due to the Gd-O vibrations of cubic Gd_2O_3. The infrared absorbtion band values represented in tabular form as shown below:

Table 3: Infrared absorption bands and their assignements.

Wave number (cm^{-1})	**FTIR Assignemnet**
450-495, 503	Bi-O bonds in [BiO_6] structural units
610-620	Bi-O bonds of different lengths in the distorted BiO_6 polyhedra
717-725	Symmetric streching vibration of Bi-O bonds in [BiO_3]
767-780	V-O-V symmetric stretching
1023	Streching vibration of V-O

The intensity of the Bi_2O_3 and V_2O_5 bands in the FTIR spectra decreases with the increasing dopant concentration for both La and Gd doped samples. The vibrational bands are quiet sharp for x=0.1 doping samples but starts diffusing as the concentration of the dopants increase. After x=0.1, the secondary phases start appearing in the samplesleads to more crystalline disorder. Due to the presence of secondary phases the vibration bands may be appeared diffused in shape. Moreover, the bans are more diffused in Gd samples as compared to La doped samples. In

addition to this, the FTIR bands are observed at lower wave number in case of La doped samples than Gd doped samples. It is well reported in the literature that the addition of higher atomic number elements shift towards to lower wave number [50]. However, in the present case, the opposite trend has been observed. It might be ascribed due to higher strain conditions prevailed in Gd doped samples.

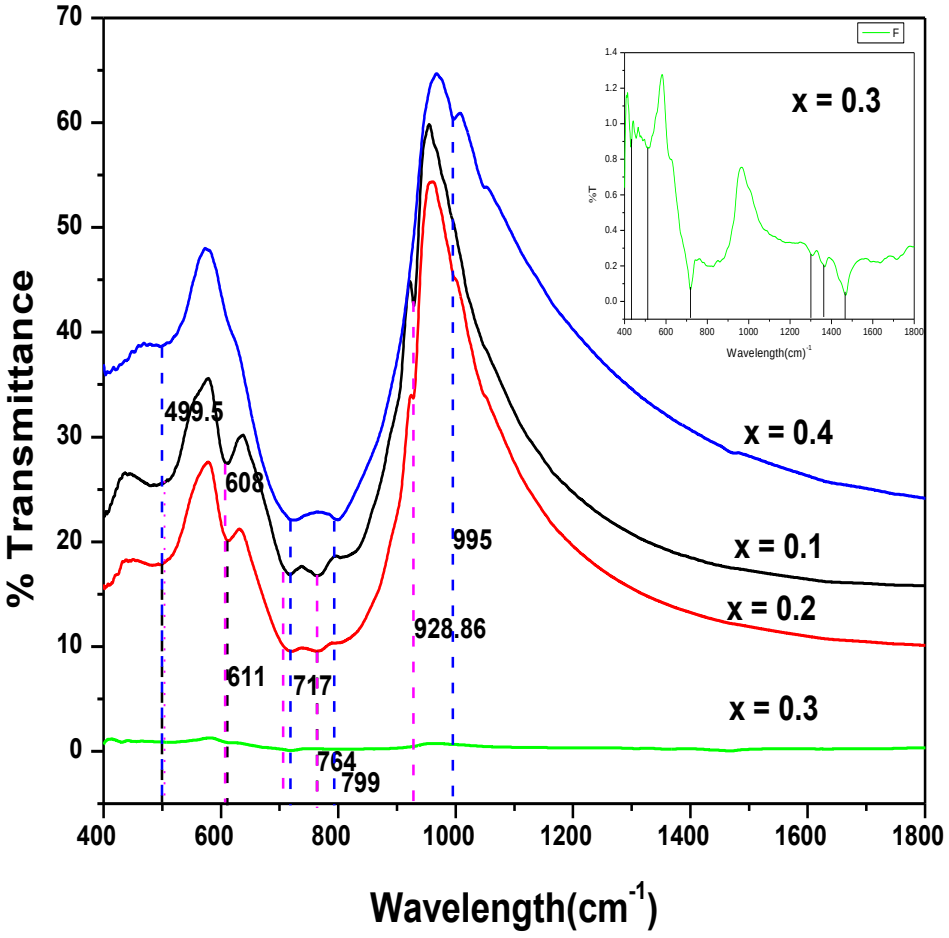

Figure 4.9: FTIR spectra of $Bi_{4-x}Gd_xV_2O_{11}$ (0≤x≥0.4).

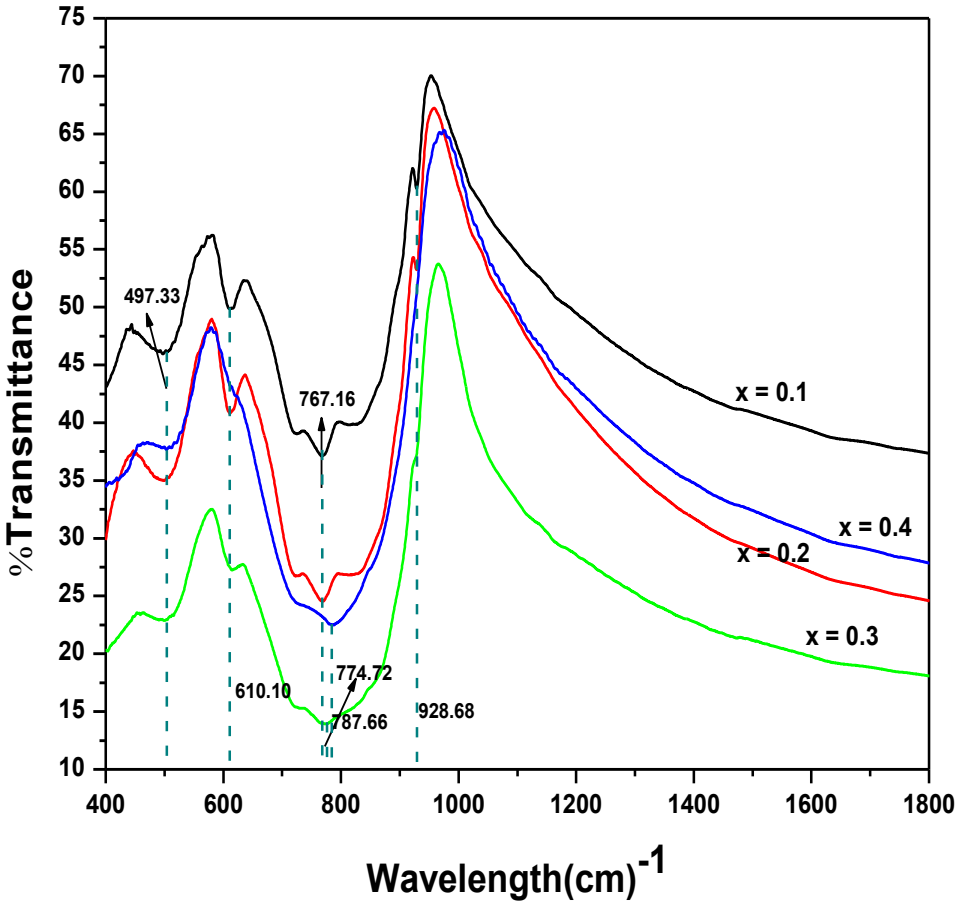

Figure 4.10: FTIR spectra of $Bi_{4-x}La_xV_2O_{11}$ ($0 \leq x \geq 0.4$).

4.1.4 Band Gap Measurement

UV-Vis spectroscopy was used to determine the band gap of $Bi_{4-x}Gd_xV_2O_{11}$ and $Bi_{4-x}La_xV_2O_{11}$ (where x = 0.1, 0.2, 0.3, and 0.4). The band gap of the semiconductors affected with the temperature, crystal structures, and elemental compositions and also depending on the processing conditions. The band gap of more stable monoclinic and tetragonal phase was 2.4 eV and 3.1 eV

of $BiVO_4$ reported by Silva. The energy band gap of the semiconductors can be calculated using equation (1)

$$\alpha h\nu = A (h\nu - E_g)^n \quad \ldots\ldots\ldots\ldots\ldots\ldots\ldots\ldots\ldots\ldots (1)$$

Where α is the absorption coefficient, h is planck's constant, ν is frequency, E_g is optical band gap and n is a constant associated to different types of electronic transitions n = ½, 2, 3/2 or 3 for direct allowed, indirect allowed, direct forbidden, and indirect forbidden transitions. The variation of $(\alpha h\nu)^2$ with respect to $h\nu$ are shown in **figure 4.11, 4.12** for all the sample. The energy band gaps are calculated from the linear fitting of tails from the graph and are tabulated in **table 4.**

Table 4: Energy band gap of $Bi_{4-x}Gd_xV_2O_{11}$ and $Bi_{4-x}La_xV_2O_{11}$ ($0 \leq x \geq 0.4$).

Sample name	Band gap(E_g) in eV	Sample name	Band gap(E_g) in eV
$Bi_{3.9}Gd_{0.1}V_2O_{11}$	2.18	$Bi_{3.9}La_{0.1}V_2O_{11}$	1.86
$Bi_{3.8}Gd_{0.2}V_2O_{11}$	3.20	$Bi_{3.8}La_{0.2}V_2O_{11}$	2.22
$Bi_{3.7}Gd_{0.3}V_2O_{11}$	2.49	$Bi_{3.7}La_{0.3}V_2O_{11}$	2.91
$Bi_{3.6}Gd_{0.4}V_2O_{11}$	1.87	$Bi_{3.6}La_{0.4}V_2O_{11}$	3.11

The band gap of pure $Bi_4V_2O_{11}$ is reported around 2 eV [35]. In case of La doped samples, the band gap has lower value for x=0.1 doping system as compared to pure $Bi_4V_2O_{11}$ system. For $x \geq 0.1$ the value of optical band increases. This may be due to either defect formation or due to the solid solution limit for La doped $Bi_4V_2O_{11}$ which is upto x=0.1. For Gd doped samples the band gap values increases upto x=0.2 and after that decreases. On the other hand, in La doped

samples with increasing dopants the band gap increases. The present band gap results are compared to the conductivity data as reported by Deepti et al. [44]. In case of La^{3+} doped samples, the conductivity increases upto x=0.1 after that shows decreasing trend. On the other hand Gd samples, show the initially increasing trend upto x = 0.2 samples as shown in **table 4.** Similar trend has been observed in the conductivity data of the Gd doped samples [44]. It also manifests that the present samples are also having some electronic contribution, in addition to ionic conduction.

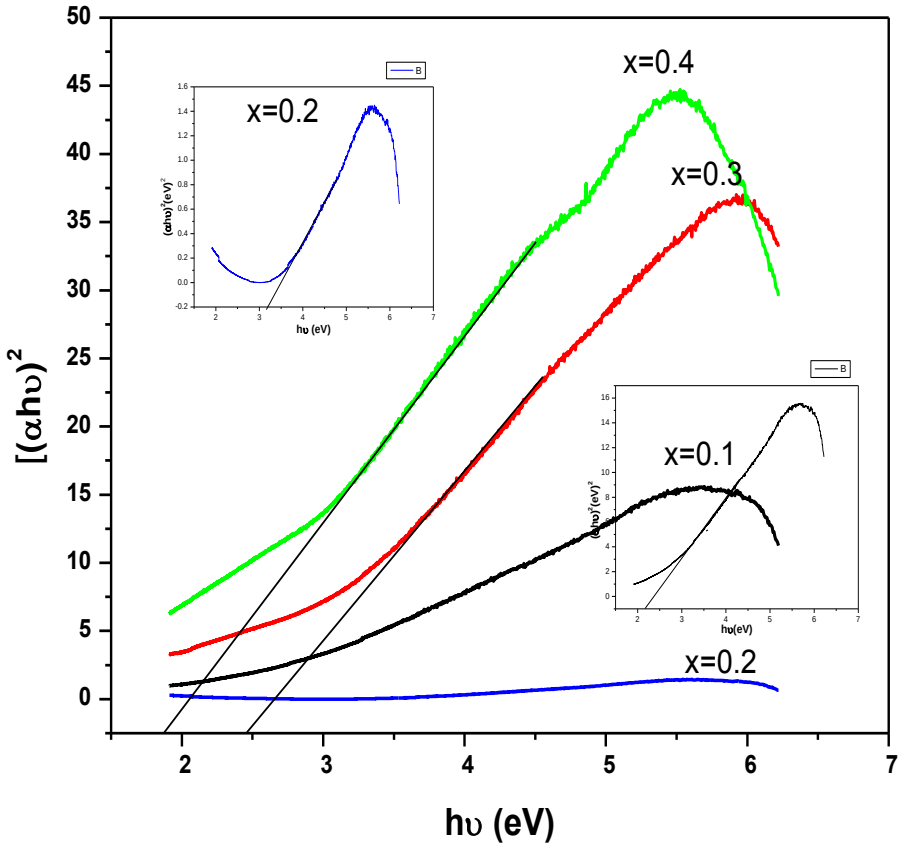

Figure 4.11: UV- Vis spectra of $Bi_{4-x}Gd_xV_2O_{11}$ samples ($0 \leq x \geq 0.4$).

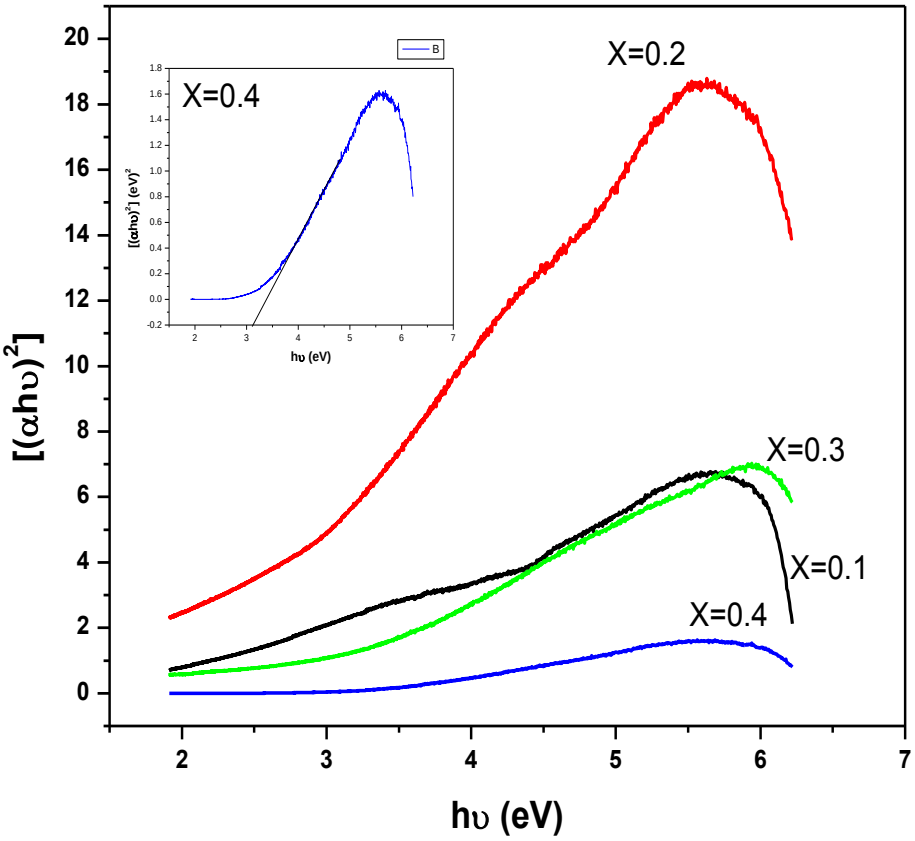

Figure 4.12: UV- Vis spectra of $Bi_{4-x}La_xV_2O_{11}$ samples ($0 \leq x \geq 0.4$).

CONCLUSION

The present work carried out to study the structural as well as optical behavior of $Bi_{4-x}M_xV_2O_{11}$ (M=La, Gd $0 \leq x \geq 0.4$) sample, by using XRD, SEM, EDS, UV-Vis spectroscopy techniques. The XRD spectra show the doublets characteristics peaks. Except x=0.4, all the samples could be indexed with α- $Bi_4V_2O_{11}$ [51]. At x=0.4, the samples could be indexed as β- $Bi_4V_2O_{11}$ due to impurity concentration so the α- phase is converting into β- phase and the overall volume of the unit cell remains constant up to x= 0.2 and after that decreases. The secondary phase of the sample observed in XRD as well as SEM spectrum, it is Bi_2O_3, La_2O_3 and Gd_2O_3. But La_2O_3- phase as an impurity phase could not observed due to the large difference of ionic radii between Bi and La. Also the calculated grain size varies in the range of 3 to 7μm. At x=0.1, both samples exhibit sharp vibrational band in FTIR and the solid solubility limit for the dopant Gd and La is observed upto 0.2 and 0.1, respectively. The band gap of $Bi_{3.6}Gd_{0.4}V_2O_{11}$ and $Bi_{3.9}La_{0.1}V_2O_{11}$ is lowest among all the samples, which shows the highest conductivity as reported by Deepti et al. [44]. The dopant effect is also observed on grains growth. The Gd doped samples has higher grain size as compare to ionic conductivity point of view.

FUTURE SCOPE

After analysis the data, the following suggestions are recommended for further investigations: Structural analysis of $Bi_{4-x}M_xV_2O_{11}$ will help to the detailed analysis of bismuth site substitution; Defects chemistry, in the compound helps to give quantitatively analysis of oxygen vacancies, which is useful for conductivity; Photocatalytic properties of $Bi_{4-x}M_xV_2O_{11}$ (M=La, Gd $0 \leq x \geq 0.4$) are strongly influence by the way of preparation and its crystal structure so more detailed investigation is required to establish exact solid solubility limit of the present samples.

REFERENCES

[1]. V.Garcia-Montalvo, R. Cea-Olivares, et al., Inor. Chem., 35, 3948 (1996).

[2]. J.D. Brown, J. Solid State Chem., 11, 214 (1974).

[3]. R. Enjalbert, R.Sorokina, S. Castro & J. Galy, Acta Chemi. Scandinavica, 49, 813 (1995).

[4]. B. Aurivillius, Ark. Kemi., 1, 54, 469 (1949).

[5]. I. Radosavljevic, J.S.O. Evans and A.W. Sleight, J. Alloys & Compds., 284, 99, (1999).

[6]. J. Huang, Q. Gu And A.W.Sleight, J. Solid State Chem., 110, 226 (1994).

[7]. A.R. West, Basic Solid State Chemistry, 2d Edition, John Wiley & Sons, 1996.

[8]. J. Huang and A.W. Sleight, J. Solid State Chem., 104, 52 (1993).

[9]. E.C. Subbarao, J. Chem. Phys., 34/2, 695 (1961).

[10]. K. Aizu, J. Phys. Soc. Japan, 27/2, 287 (1969).

[11]. J.D. Bierlein and A.W. Sleight, Solid State Commun, 16, 69 (1975).

[12]. T. Takahashi And H. Iwahara, Mat. Res. Bull., 13, 1447 (1978).

[13]. G.Mairesse, Fast Ion Transp.In Solids, Edited By B. Scrosati, Kluver Amsterdam, (1993).

[14]. F. Abraham, M.F. Debreuille-Gresse, et al. Solid State Ionics, 28/30, 529 (1988).

[15]. A. Watanabe, Solid State Tonics, 96, 75 (2997).

[16]. A.W. Sleight, Science, 242, 1519 (1988).

[17]. A.W. Sleight, J.L. Gillson and P.E. Bierstedt, Solid State Commun. 17, 27 (1975).

[18]. S.K. Poznyak, V.V. Sviridov and A.I. Kulak, Elektrokhimiya, 20/7, 996 (1984).

[19]. Qurashi M.M., Barnes W.H, Amer. Mineralogist, 38 (1953), 489.

[20]. Cox D.E.,Moodenbaugh A.R., Sleight A.W., Chen H.Y., Nbs Spe. Pub., 567 (1980), 189.

[21]. Abraham F., Debreuille-Gresse M.F., et al. Solid State Ionics, 28–30(1988), 529.

[22]. Watanabe A., J. Solid State Chem., 161 (2001), 410.

[23]. Watanabe A., Kitarni Y., Solid State Ionics, 113–115 (1998), 601.

[24]. Icdd Powder Diffraction File, Pdf-2, Icdd, Pennsylvania, Usa, 1998, Card 44–171.

[25]. Lee M.D., Chen W.S., Chiang H.P., Appl. Catal. A., 101 (1993), 269.

[26]. Abraham F., Boivin J.C.,Mairesse G., et al. Solid State Ionics, 40/41 (1990), 934.

[27]. G. Gattow et al., Zeitschrift fur Anorganishe und Allgemeine Chemie, 318 (1962) 176.

[28]. T. Takahashi, T. Esaka and H. Iwahara, J. Of Appl. Electrochem, 7 (1977) 31.

[29]. Aurivillius B., Ark Kemi. 1 (1949) 463.

[30]. Aurivillius B., Ark Kemi. 1 (1949) 499.

[31]. I. Abrahams And F. Kork, J. Mater. Chem., 12 (2002), 3351-3362.

[32]. B. Frit And J. P. Mercurio, J. Alloys Comp.188 (1992) 27.

[33]. T. Kikuchi, Mater. Res. Bull. 14 (1979) 1561.

[34]. K.R. Kendall, C. Navas, J.K. Thomas & H.C. Zur Loye, Chem. Mater., 8 (1996) 642.

[35]. Vaishali Thakral, S. Uma, Material Research Bulletin 45 (2010) 1250-1254.

[36]. J. Huang and A.W. Sleight, Physica C, 169, 169 (1990).

[37]. Y.L.Yang, L. Qiu, W. T. A. Harrison, et al. J. Mater. Chem.7 (2) (1997) 243.

[38]. Neelam Kumari, S.B. Krupanidhi, K.B.R. Varma J. Mater.Sci.45 (2010) 464-473.

[39]. S. Kohtani, J. Hiro, et al. Catal. Commun.6 (2005) 185–189.

[40]. Lingzhi Li, Bing Yan J. Optoelectronics and Adv. Mat., 10 (2008)P. 2738 – 2742.

[41]. Hongmei Luo, Alexh.Mueller, et al. J.Phys.Chem.C 2008, 112, 6099 6102.

[42]. Hui Xu[a], Huaming Li[b,*] et al. Journal of hazardous materials 153(2008)877–884.

[43]. Neelam Kumari, S.B. Krupanidhi, K.B.R. Varma J. Mater.Sci.45 (2010) 464-473.

[44]. Deepti, Ravikant, M.L.Singla, K. Singh Current Applied Physics 9 (2009) 1467-1473.

[45]. Zhang A. And Zhang J. Materials Science-Poland, 27, 4/1, 2009.

[46]. Aiping Zhang, Jinzhi Zhang J.Mater. Sci. 45(2010) 4040-4045.

[47]. Yingna Guo, Xia Yang, Fengyan Ma, et al. App. Surface Sci. 256(2010) 2215-2222.

[48]. A.Fernandez-Osorio, A. Cervantes-Macias, et al. Cancun. Q.R.Mexico. 26-29, 2010.

[49]. Mirela Dragomir, Matjaz Valant, Uni of Nova Gorica, Vipavaka 13, Slovenia.

[50]. G. Kaur. O.P. Pandey, And K. Singh, Physica Status Solidi 2012.

[51]. O. Joubert, M. Ganne, et al. J. Sloid State Ionics, 83 (1996), 199-207.

[52]. Meenu Singh, Jasmeet Kaur Gill et al. Ionics 18 (2012) 479-486.

[53]. I. Ardelean, et al. Journal of Optoel. & Adv. Mat. 8, 5, (2006) 1843-1847.